Biosensors and Bioelectronics 148 (2020) 111739

Contents lists available at ScienceDirect

Biosensors and Bioelectronics

journal homepage: http://www.elsevier.com/locate/bios

# Photoelectrochemical competitive immunosensor for 17β-estradiol detection based on $ZnIn_2S_4$@$NH_2$-MIL-125(Ti) amplified by PDA NS/Mn:ZnCdS

Tao Yan [a], Tingting Wu [a], Shiyuan Wei [a], Haoqi Wang [a], Meng Sun [a], Liangguo Yan [a], Qin Wei [b,*], Huangxian Ju [b,c]

[a] School of Water Conservancy and Environment, University of Jinan, Jinan, 250022, PR China
[b] Key Laboratory of Interfacial Reaction & Sensing Analysis in Universities of Shandong, School of Chemistry and Chemical Engineering, University of Jinan, Jinan, 250022, China
[c] State Key Laboratory of Analytical Chemistry for Life Science, Department of Chemistry, Nanjing University, Nanjing, 210023, PR China

ARTICLE INFO

*Keywords:*
PEC competitive immunosensor
$ZnIn_2S_4$@$NH_2$-MIL-125(Ti) composite
PDA NS/Mn:ZnCdS QDs
17β-estradiol

ABSTRACT

A competitive-type PEC immunosensor for 17β-estradiol ($E_2$) detection was successfully fabricated using $ZnIn_2S_4$@$NH_2$-MIL-125(Ti) composite as matrix. The excellent PEC behavior of $ZnIn_2S_4$@$NH_2$-MIL-125(Ti) composite could be attributed to that the $Ti^{4+}$-$Ti^{3+}$ intervalence cycles in the titanium oxo-cluster of $NH_2$-MIL-125(Ti) as well as the matching energy level between $ZnIn_2S_4$ and $NH_2$-MIL-125(Ti) promote the migration and separation of photocarrier. Besides, polydopamine (PDA) with abundant amino- and quinone-groups was selected to further improve the PEC signals and capture antibody, which implement through the covalent bonding of PDA and BSA-$E_2$ or carboxyl-group functionalized Mn:ZnCdS QDs in the competitive-type strategy. Concretely, the quinone functional groups in PDA film was applied to immobilize BSA-$E_2$ through Michael reactions, and the PDA nanosphere loaded Mn:ZnCdS quantum dot (PDA NS/Mn:ZnCdS QDs) was used as antibodies' labels to amplify PEC signals. After PDA NS/Mn:ZnCdS-anti-$E_2$ immobilized on the modified electrode, a remarkable increase of photocurrent signal was observed owing to the specific bonding of antigen and antibody. Based on the competitive binding of PDA NS/Mn:ZnCdS-anti-$E_2$ with either free $E_2$ or bovine serum albumin (BSA)-$E_2$ causing the change of the photocurrent signal, the standard sample free $E_2$ could be accuracy detect. Under optimal conditions, the competitive-type PEC immunosensor exhibited the linear range from 0.0005 ng/mL to 20 ng/mL and a limit detection of 0.3 pg/mL (S/N = 3). Meanwhile, the acceptable stability, selectivity and reproducibility of the proposed PEC immunosensing platform indicating the promising detection of small molecular environmental pollutants.

## 1. Introduction

17β-estradiol ($E_2$), a typical endogenous estrogen, is in charge of the growth and development of the female reproductive system (Singh et al., 2017). It is widely exist in environment due to the residual in female hormone drug production or the metabolism of organisms (Li et al., 2011). Researchers have proved that trace levels of $E_2$ can cause immune deficiency and increase the risk of ovarian and breast cancer in women (Ming et al., 2017). Due to its strong bioaccumulative toxicity, $E_2$ has been added to the group of environmental endocrine disrupting chemical (EDC) (Han et al., 2016). Until now, various analytical methods have been developed for the detection of $E_2$, such as electrochemical analyses (Zhang et al., 2014), liquid chromatography (Hao et al., 2015), magnetic sensing film (Han et al., 2016) and capacitive immunosensor (Singh et al., 2017). However, most of the mentioned methods usually have the drawbacks including time-consuming, bulky instruments and expensive. Thus, it is imperative to develop a simple, low cost and rapid $E_2$ analysis methods.

Photoelectrochemical (PEC) sensing has developed rapidly for the detection of biological and environmental molecules owing to its low background noise, low cost, acceptable stability and ease of miniaturization (Fan et al., 2015; Han et al., 2017; Shu et al., 2016). The kernel

* Corresponding author.
*E-mail address:* sdjndxwq@163.com (Q. Wei).

https://doi.org/10.1016/j.bios.2019.111739
Received 2 September 2019; Accepted 27 September 2019
Available online 28 September 2019

component of PEC sensors is photochemically active material which can convert light excitation energy to an electrical signal (Wu et al., 2018b). So far, a variety of semiconductor materials including metal sulfides (Zhao et al., 2014), metal oxides (Zhang et al., 2017b), novel carbon-based materials (Zeng et al., 2013) have been explored for fabricating PEC sensor. However, the photoelectric activity over these materials are restricted because the poor separation efficiency of photogenerated carriers and the inefficient utilization efficiency of solar energy. Consequently, it is an inevitable trend to explore high-efficiency photoactive materials.

Metal organic framework (MOFs), a class of crystalline micro-mesoporous hybrid materials with metal units assembling with organic ligands. In the past two decades, MOFs as a preeminent all-round and adjustable platform have received a large amount of attention from researchers, which mainly owing to their ultrahigh porosity and internal surface areas (Wu et al., 2018a). MOFs have shown great promise in many diverse applications, such as catalysis (Fu et al., 2012), sensing (Zhang et al., 2016), gas storage/separation (Ma et al., 2009) and drug delivery (Peng et al., 2014), etc. It has been reported that some MOFs possess semiconducting performance and can act as a charge-carrier transport system in PEC sensing (Zhan et al., 2013; Zhang et al., 2016). In addition, the abundant pore structures of MOFs are propitious to the enrichment of target analyte which can improve the performance of the sensors (Jin et al., 2017). Recently, various semiconductor@MOFs structures have been synthesized including $Cd_{0.2}Zn_{0.8}S$@UiO-66-$NH_2$ (Xie et al., 2017), $TiO_2$@$NH_2$-MIL-125(Ti) (Li et al., 2018), ZnO@ZIF-8 (Zhan et al., 2013) and $Ni_2P$/MIL-125-$NH_2$ (Kampouri et al., 2018). Among them, Ti-based MOFs have been widely applied because it not only contains unparalleled characters of MOFs but also has attractive redox and photocatalytic properties (Hendon et al., 2013). The $Ti^{4+}$-$Ti^{3+}$ intervalence cycles in the titanium oxo-cluster contributes to the efficient transfer of photo-induced electron (Li et al., 2018).

As a ternary chalcogenide, $ZnIn_2S_4$ has attracted increasing attention owing to its suitable bandgap (~2.6 eV), excellent visible-light-response and outstanding stability (Liu et al., 2018). For example, Chen et al. prepared hexagonal $ZnIn_2S_4$ microspheres and cubic $ZnIn_2S_4$ nanoparticles *via* a hydrothermal process, and compared the photocatalytic activity in the degradation of Rhodamine B (RhB) (Chen et al., 2012). Tan et al. reported that Sm-doped $ZnIn_2S_4$ microspheres was successfully prepared by doping samarium into $ZnIn_2S_4$, the obtained Sm-doped $ZnIn_2S_4$ exhibited a remarkable photoactivity for the degradation of RhB (Tan et al., 2014).

Herein, we choose $ZnIn_2S_4$ coupling with $NH_2$-MIL-125(Ti) as PEC sensing material. The $Ti^{4+}$-$Ti^{3+}$ intervalence cycles in the titanium oxo-cluster as well as the matching energy level between $ZnIn_2S_4$ and $NH_2$-MIL-125(Ti) effectively facilitate the separation of electron-hole pairs. To achieve the competitive detection of $E_2$, the PDA NS/Mn:ZnCdS QDs were covalently conjugated with anti-$E_2$ as labels. The dopant of Mn can introduce an electronic state in the mid-gap region of the QDs which depress the charge recombination (Zhang et al., 2017a). Moreover, PDA NS with surface functional groups (-$NH_2$) could capture more Mn:ZnCdS QDs through the interaction between the amino groups and carboxyl groups.

## 2. Experimental section

### 2.1. Materials and reagents

2-$NH_2$-terephthalic acid ($H_2ATA$) was obtained from Macklin Biochemical Co., Ltd. (Shanghai, China). Bovine serum albumin (BSA)-$E_2$, 17β-estradiol ($E_2$) and anti-estradiol (anti-$E_2$) were both purchased from Shenzhen Anti Biotechnology Co., Ltd. The other details are provided in the Supplementary Material.

### 2.2. Apparatus

Energy dispersive spectrometer (EDS) images were obtained from emission scanning electron microscope (SEM) (Zeiss, Germany). Transmission electron microscopy (TEM) and high-resolution transmission electron microscopy (HRTEM) images were obtained from a JEOL-2100F TEM (Japan). The other details are provided in the Supplementary Material.

### 2.3. Preparation of $NH_2$-MIL-125(Ti) and $ZnIn_2S_4$@$NH_2$-MIL-125(Ti) composite

$NH_2$-MIL-125(Ti) was prepared by a one-step solvothermal method. First, 3.0 g $H_2ATA$ and 1.56 mL $Ti(OC_4H_9)_4$ were dissolved into a solution containing 54 mL DMF and 6 mL MeOH with magnetic stirring for 60 min. And then, the above mixture was transferred into Teflon-lined stainless-steel autoclave and heated at 150 °C for 24 h. After cooling to room temperature, the obtained products were washed with methanol and DMF for several times, collected by centrifugation and dried under vacuum.

$ZnIn_2S_4$@$NH_2$-MIL-125(Ti) composite was synthesized according to the literature with minor modifications (Liu et al., 2018). A certain amount of $NH_2$-MIL-125(Ti) was dispersed in a mixture solution of 15 mL DMF and 5 mL MeOH glycerol. After ultrasound for 10 min, 0.136 g $ZnCl_2$, 0.30 g TAA and 0.442 g $InCl_3$ were added to the above solution and stirred for 1 h. After that, the final suspension was transferred to a Teflon-lined autoclave and heated at 180 °C for 10 h. The resulting mixture was washed with distilled water and ethanol for several times and dried at 60 °C. The as-synthesized $ZnIn_2S_4$@$NH_2$--MIL-125(Ti) samples with different $NH_2$-MIL-125(Ti) mass ratios of 1, 3, 5, 10 and 20% have been synthesized and designated as ZIS@NM1, ZIS@NM3, ZIS@NM5, ZIS@NM10 and ZIS@NM20, respectively.

### 2.4. Preparation of PDA NS/Mn:ZnCdS-anti-$E_2$ bioconjugates

PDA NS was synthesized by oxidative polymerization of dopamine based on previous reports (Yan et al., 2013). Carboxyl groups functionalized Mn:ZnCdS QDs was prepared according to the previous reports with slight modification (He et al., 2016). The other details are provided in the Supplementary Material.

### 2.5. Fabrication of the immunosensor for detecting $E_2$

The fabrication procedure of the immunosensor was shown in Scheme 1. Before fabrication, indium-tin-oxide (ITO) slices were cut into $2 \times 0.8\ cm^2$ sections and washed separately with acetone, ethanol, and ultrapure water for 30 min. Subsequently, the ITO slices were dried under a nitrogen stream.

First, 10 μL 4 mg/mL ZIS@NM3 was dropped onto the ITO electrode and dried at room temperature. Then 5 μL 0.5 mg/mL dopamine Tris-HCl solution (pH = 8.5) was decorated on the ZIS@NM3/ITO electrode for 1 h to form the PDA film by self-polymerization of dopamine. After washed thoroughly, 5 μL BSA-$E_2$ was attached to modified electrode with PDA film being used as bridging media. Concretely, the quinone functional groups in the PDA could directly couple with amine-terminated biomolecules *via* Michael addition (Wang et al., 2017a). The electrode was incubated at 4 °C and then rinsed with washing buffer. In order to block nonspecific binding sites, 5 μL 1% bovine serum albumin (BSA) was incubated on the electrode at 4 °C for 1 h. Finally, after washed with washing buffer, 5 μL mixing solution of PDA NS/Mn:ZnCdS-anti-$E_2$ and $E_2$ was dropped onto electrode surface and incubated at 4 °C for another 1 h. The resulting electrodes were washed and stored at 4 °C until testing.

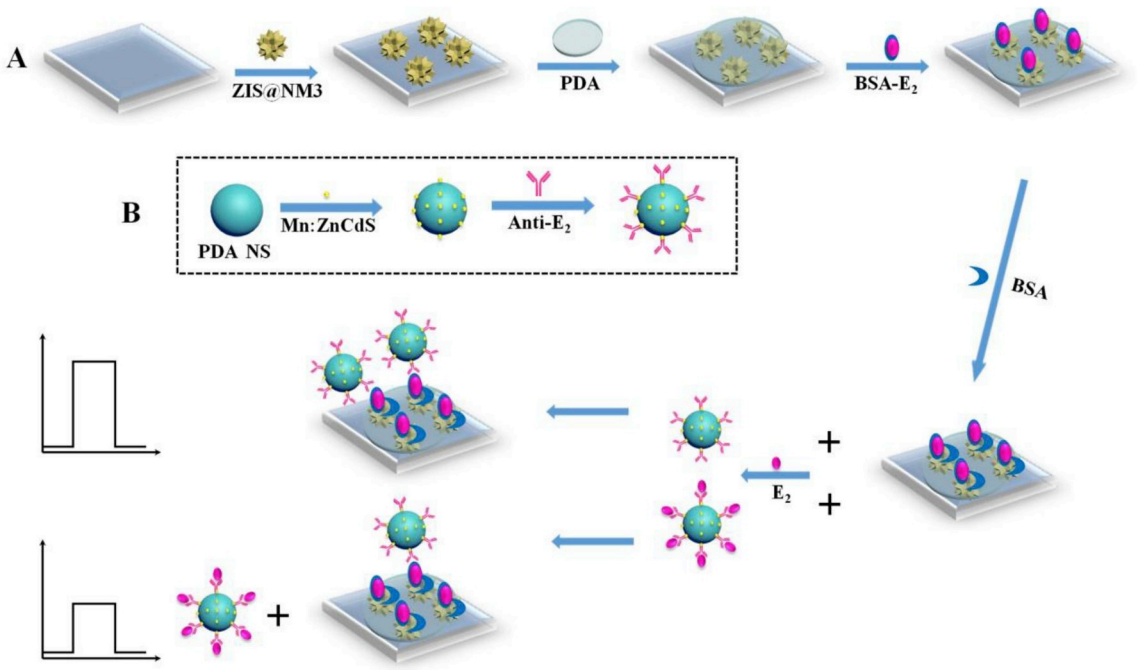


**Scheme 1.** (A) Fabrication procedure of a PEC immunosensor for detection of $E_2$; (B) Preparation procedure of PDA NS/Mn:ZnCdS-anti-$E_2$ bioconjugates.

### 2.6. PEC detection

PEC detection was carried out in 0.1 mol/L phosphate buffered saline (PBS, pH = 7.4) containing 0.2 mol/L ascorbic acid (AA) which was served as sacrificial electron donor. The photocurrent was measured on PEC workstation (Zahner Zennium PP211, Germany) with a conventional three-electrode system. The light intensity was 150 W/cm$^2$ with wavelength of 450 nm. Bias voltage was 0 V.

## 3. Results and discussion

### 3.1. Characterization of the synthesized materials

The morphologies and microstructures of prepared materials were characterized by SEM and TEM. As shown in Fig. 1A, $NH_2$-MIL-125(Ti) has rod-like shape and the length was about 100 nm which is different from previously reported (Liu et al., 2018) due to different ratio of raw materials. In addition, pristine $ZnIn_2S_4$ possesses a microsphere morphology with average diameter about 1 μm (Fig. 1B). After hybridization, $ZnIn_2S_4$ microspheres were unfolded (Fig. 1C and D) and $ZnIn_2S_4$@$NH_2$-MIL-125(Ti) composite was smaller than $ZnIn_2S_4$. The tight contact between $ZnIn_2S_4$ and $NH_2$-MIL-125(Ti) could promote the transfer of electron. The EDS analysis in Fig. 1G indicated that C, N, O, Ti, Zn, In, S elements were observed in $ZnIn_2S_4$@$NH_2$-MIL-125(Ti) composite. The elemental mapping images of $ZnIn_2S_4$@$NH_2$-MIL-125 (Ti) composite in Fig. S1 showed that C, N, O, Ti, Zn, In, S elements were well defined with sharp contrast. It can be observed from Fig. 1E, Mn:ZnCdS QDs was uniformly distributed on PDA NS, and HRTEM image (Fig. 2F) of PDA NS/Mn:ZnCdS QDs further confirmed the crystallite size of Mn:ZnCdS QDs is ~3 nm. Fig. S2A shows the EDS spectrum, which illustrates the Mn:ZnCdS QDs is composed of Mn, Zn, Cd, S elements.

The XRD analyses of $ZnIn_2S_4$, $NH_2$-MIL-125(Ti) and $ZnIn_2S_4$@$NH_2$-MIL-125(Ti) composite were given in Fig. 1H. For pristine $ZnIn_2S_4$ (curve a), the reflection peaks appearing at 21.1°, 27.7° and 47.8° could be assigned to the hexagonal $ZnIn_2S_4$ (JCPDS No.65–2023) (Shang et al., 2013). Curve c shows that the XRD pattern of $NH_2$-MIL-125(Ti) coincide with previous reports (Fu et al. 2012, 2016). For $ZnIn_2S_4$@$NH_2$-MIL-125 (Ti) (curve b), the diffraction peaks at 6.4° and 9.7° were attributed to $NH_2$-MIL-125(Ti), which confirmed $ZnIn_2S_4$@$NH_2$-MIL-125(Ti) was successfully prepared. For Mn:ZnCdS QDs (Fig. S2B), the diffraction peaks at 26.8°, 44.5° and 52.6° could be indexed to (111), (220) and (311) planes of ZnCdS QDs (Ouyang et al., 2007). It is worth noting that the crystal structure of ZnCdS has not changed after doping of Mn and the diffraction peak of Mn species was not obtained, which could be due to the small quantity of Mn.

X-ray photoelectron spectrometry (XPS) was used to characterize the chemical states of $ZnIn_2S_4$@$NH_2$-MIL-125(Ti). The full XPS spectra of $ZnIn_2S_4$@$NH_2$-MIL-125(Ti) in Fig. 1I showed that only C, N, O, Ti, S, In, Cd elements existed in the sample, which coincided with EDS spectrum. The C 1s spectrum in Fig. S3A could be divided into four peaks, located at 284.6 eV, 285.6 eV, 286.6 eV and 288.8 eV which assigned to C═C, C–N, C–C, and C═O of $H_2$ATA (Wang et al. 2015a, 2015b). In the N 1s spectrum (Fig. S3B), the peaks at 399.4 eV and 402.3 eV could ascribable to the N of the amine functionality stretching out or protruding into the cavities and the positively charged nitrogen (–N = $^+$ and –NH–$^+$) (Wang et al. 2015a, 2015b). In the O 1s spectrum (Fig. S3C), three peaks could be observed. The peaks appeared at 530.0 eV and 532.6 eV can be indexed to C═O and oxygen in titanium oxo-cluster, respectively. The peaks appeared at 532.7 eV showed presence of hydroxyl groups (Wang et al., 2015a). As shown in Fig. S3D, peaks for Ti $2p_{3/2}$ and Ti $2p_{1/2}$ at 458.4 eV and 464.3 eV suggesting titanium bounded to oxygen remains in oxidation state IV for the titanium oxo-cluster. Two separated peaks at 161.5 eV and 162.7 eV in the high-resolution XPS spectrum of S 2p (Fig. S3E) could be ascribed to S $2p_{3/2}$ and S $2p_{1/2}$, respectively (Yuan et al., 2016). As presented in Fig. S3F, the peaks at 444.6 eV and 451.5 eV are assigned to In $3d_{5/2}$ and In $3d_{3/2}$, respectively (Lin, 2014). Two peaks recorded in the Zn 2p region at 1021.4 and 1044.4 eV could be assigned to Zn $2p_{3/2}$ and Au $2P_{1/2}$, respectively (Fig. S3G).

### 3.2. Mechanism exploration

The optical absorption characteristics of as-prepared samples were measured by UV–vis diffuse reflectance spectra. As shown in Fig. S4A, for $NH_2$-MIL-125(Ti), two absorption edges around at 350 nm and 525 nm were ascribed to the absorption of titanium oxo-clusters and the ligand-based absorption, respectively (Fu et al. 2012, 2016). It could be observed that the absorption edge of $ZnIn_2S_4$ was located at 600 nm. Compared with $NH_2$-MIL-125(Ti), the absorption edges of

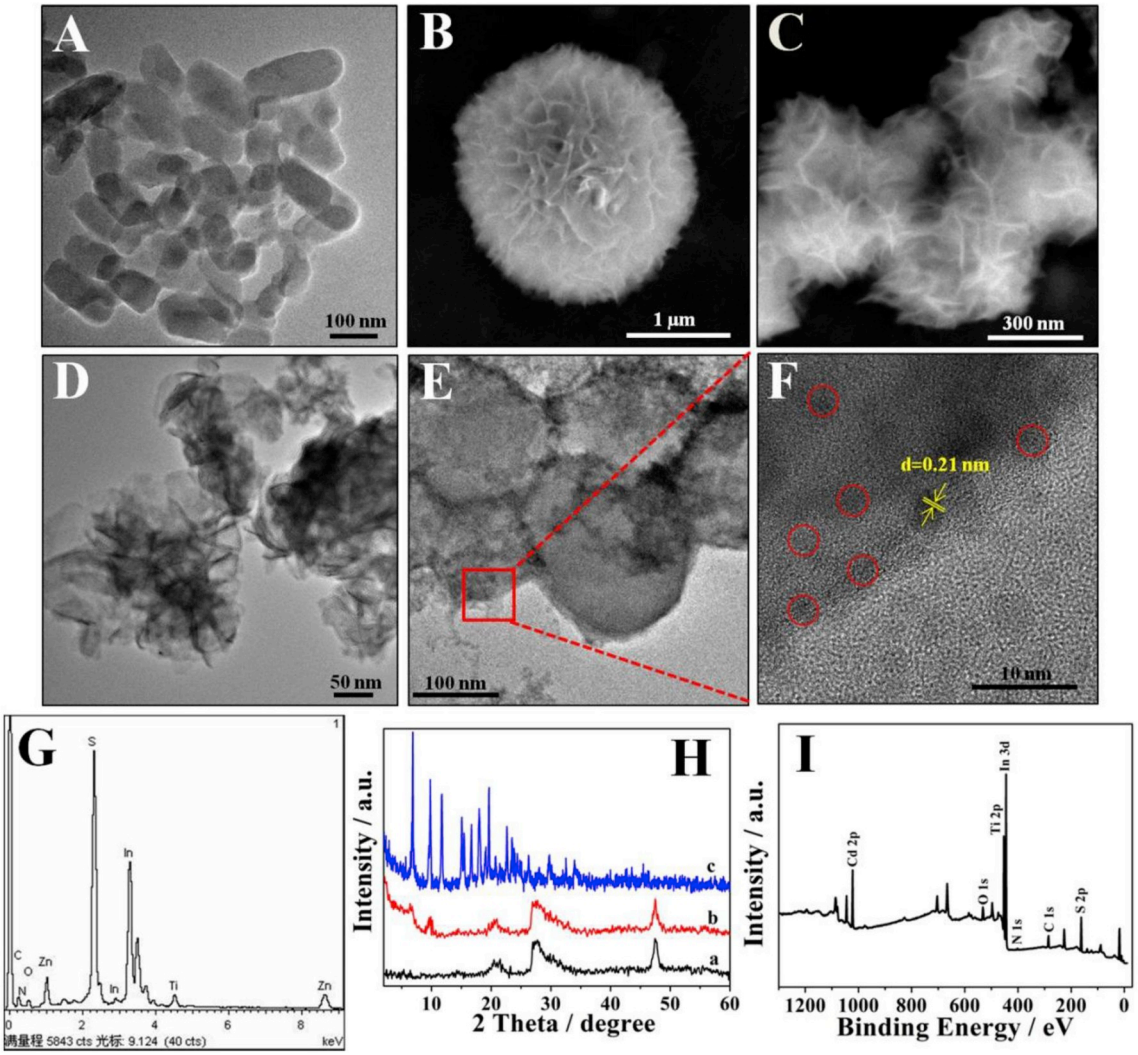


**Fig. 1.** TEM image of $NH_2$-MIL-125(Ti) (A); SEM image of $ZnIn_2S_4$ (B); SEM image (C) and TEM image (D) of $ZnIn_2S_4$@$NH_2$-MIL-125(Ti); TEM image (E) and HRTEM (F) image of PDA NS/Mn:ZnCdS QDs; EDS spectrum of $ZnIn_2S_4$@$NH_2$-MIL-125(Ti) (G); XRD patterns of $ZnIn_2S_4$ (curve a), $ZnIn_2S_4$@$NH_2$-MIL-125(Ti) (curve b) and $NH_2$-MIL-125(Ti) (curve c) (H); XPS spectra of $ZnIn_2S_4$@$NH_2$-MIL-125(Ti) (I).

$ZnIn_2S_4$@$NH_2$-MIL-125(Ti) composite showed a red shift, illuminating that the composite could utilize more visible light. In addition, Fig. S4B showed that the absorption edge of ZnCdS was 540 nm, while that for Mn:ZnCdS was 565 nm.

The flat-band potential of prepared materials was obtained by Mott-Schottky plots. Fig. S5A showed that $NH_2$-MIL-125(Ti) and $ZnIn_2S_4$ were n type semiconductor and the flat-band potentials were −0.9 V vs. SCE (−0.66 V vs. NHE) and −0.98 V vs. SCE (−0.74 V vs. NHE), respectively. For n type semiconductor, the conduction band potentials ($E_{CB}$) are 0.1–0.2 V negative than flat-band potentials (Wu et al., 2018b). It could be obtained from Fig. S4A inset, the band-gap energies for $NH_2$-MIL-125 (Ti) and $ZnIn_2S_4$ were 2.65 eV and 2.3 eV. Thus, the valence band potentials ($E_{VB}$) of $NH_2$-MIL-125(Ti) and $ZnIn_2S_4$ were determined to be +1.89 V vs. NHE and +1.46 V vs. NHE. Furthermore, it has been reported that the carrier density of the electrode material was inversely proportional to the slope of the plot (Chen et al., 2017; Sultana et al., 2017). As shown in Fig. S5A, the slope of $ZnIn_2S_4$@$NH_2$-MIL-125(Ti) is much smaller than $NH_2$-MIL-125(Ti) and $ZnIn_2S_4$, indicating the higher carrier density of $ZnIn_2S_4$@$NH_2$-MIL-125(Ti). In addition, the band-gap energies of Mn:ZnCdS QDs was 2.2 eV (Fig. S4B inset) and it can be inferred from Fig. S5B that the $E_{CB}$ and $E_{VB}$ were −0.95 V vs. NHE and +1.25 V vs. NHE.

The photo-generated electrons and holes transfer mechanism of the PEC immunosensor was displayed in Scheme 2. Under visible light illumination, both $NH_2$-MIL-125(Ti) and $ZnIn_2S_4$ could be excited to generate electrons and holes. The photo-generated electrons were quickly transmitted from the CB of $ZnIn_2S_4$ to $NH_2$-MIL-125(Ti) due to the matching energy level. At the same time, electrons generated in organic ligand of $NH_2$-MIL-125(Ti) could be transferred to titanium oxo-clusters to produce $Ti^{3+}$ (Fu et al., 2012). After that, the electron could transfer to ITO generating the photocurrent response and $Ti^{3+}$ are recovered back as $Ti^{4+}$. Furthermore, when the PDA NS/Mn:ZnCdS QDs-anti-$E_2$ was attached to the photoelectrode, the current intensity increased rapidly. This could be attributed to two aspects: On one hand, the excited electrons in Mn:ZnCdS would be quickly injected into the $ZnIn_2S_4$ due to the matching of energy levels between Mn:ZnCdS and $ZnIn_2S_4$, and therefore the photoinduced electrons and holes could be separated efficiently. On the other hand, PDA NS could inhibit the photogenerated electron-hole recombination (Wang et al., 2017a). Meanwhile the photogenerated holes on the VB side of $NH_2$-MIL-125(Ti) directly move to $ZnIn_2S_4$ and then to the VB of Mn:ZnCdS and finally be scavenged by AA.

Photoluminescence (PL) emission spectrum was performed to provide useful information about separation efficiency of photogenerated electron-hole pairs (Su et al., 2017). Fig. S4C showed a strong emission peak approximately at 445 nm for $ZnIn_2S_4$. However, the PL emission

intensity for $ZnIn_2S_4$@$NH_2$-MIL-125(Ti) decreases markedly indicating the significant improvement of the separation efficiency of electron-hole pairs.

### 3.3. Characterization of the fabricated PEC immunosensor

Electrochemical impedance spectroscopy (EIS) is a powerful tool to characterize the interface properties of electrodes during the fabrication process (Li et al., 2017; Wu et al., 2016). EIS was performed in a solution containing 0.1 mol/L KCl and 2.5 mmol/L $Fe(CN)_6^{3-/4-}$. It can be seen from Fig. 2A, the impedance spectrum contained a semicircle portion at a higher frequency and a linear portion at lower frequency region. The semicircle diameter equaled to electron transfer resistance ($R_{et}$) which was an important indicator to analysis the interface properties of electrodes (Wang et al., 2017b). The inset in Fig. 2A was the equivalent circuit includes $R_{et}$, the solution resistance ($R_s$), the Warburg impedance ($Z_\omega$) and the double-layer capacitance ($C_{dl}$). The values of them simulated with *ZSimWin* software were shown in Table S1 (Supplementary Material). The bare ITO electrode exhibited a small semicircle domain, suggesting a free electron-transfer process (curve a). After ZIS@NM3 deposition, a larger semicircle diameter was obtained (curve b), which indicated successful modification of matrix materials. After the decoration of PDA film, the $R_{et}$ decreased slightly (curve c). This phenomenon could be attributed to charge transfer of the PDA (Wang et al., 2017a). When BSA-$E_2$ (curve d), BSA (curve e) and the mixing solution of free $E_2$ and PDA NS/Mn:ZnCdS-anti-$E_2$ (curve f) were immobilized, the $R_{et}$ were increased gradually due to the insulating effect of protein.

The fabrication process of PEC immunosensor could be monitored by the photocurrent response. As shown in Fig. 2B, the bare ITO electrode showed a small photocurrent (cover a). When ZIS@NM3 coated, the photocurrent intensity was obviously increased (cover b). After modified with PDA film (cover c), the photocurrent reached a maximum. This is because that PDA as electron donor could promote the separation of photogenerated electron-hole pairs (Feng et al., 2018; Fan et al., 2017). After the immobilization of BSA-$E_2$ (curve d) and BSA (curve e), the photocurrent decreased significantly. This could be attributed that the protein could obstruct the electron transfer and prevent AA reacting with the photogenerated holes. After the mixing solution of free $E_2$ and PDA NS/Mn:ZnCdS-anti-$E_2$ dropped on the electrode, the photocurrent intensity increased obviously (curve f). The inset in Fig. 2B shows that ZIS@NM3 exhibited the highest photocurrent which could be attributed to the well-matched band structure between $NH_2$-MIL-125(Ti) and $ZnIn_2S_4$ facilitated the transfer of photogenerated charges.

### 3.4. Optimization of experimental conditions

To obtain the best analytical performance for the detection of $E_2$, several experiment conditions were optimized. As shown in Fig. 3A, the

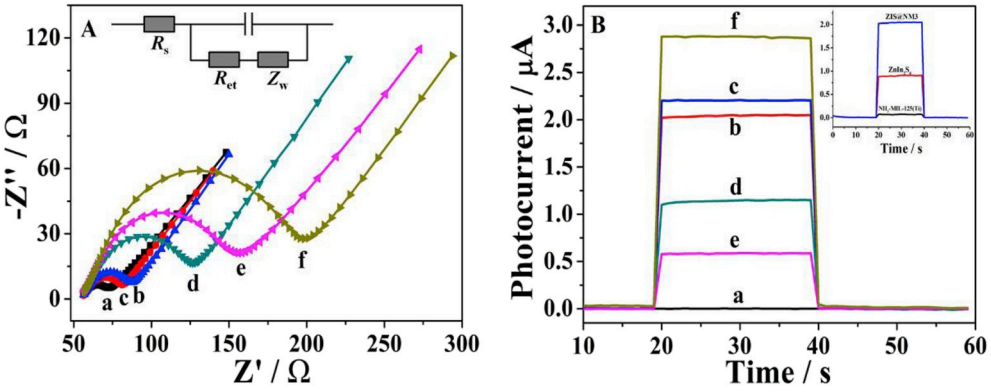


**Fig. 2.** (A) Nyquist plots of electrochemical impedance spectroscopy and (B) corresponding photocurrent responses of the modified ITO electrodes: (a) bare ITO electrode, (b) after ZIS@NM3 deposition, (c) PDA subsequently coating, (d) after BSA-$E_2$ immobilization, (e) after BSA blocking, (f) after incubation with mixing solution of free $E_2$ and PDA NS/Mn:ZnCdS-anti-$E_2$. The inset in A is the equivalent circuit for EIS and the inset in B is the photocurrent of $NH_2$-MIL-125(Ti), $ZnIn_2S_4$ and ZIS@NM3.

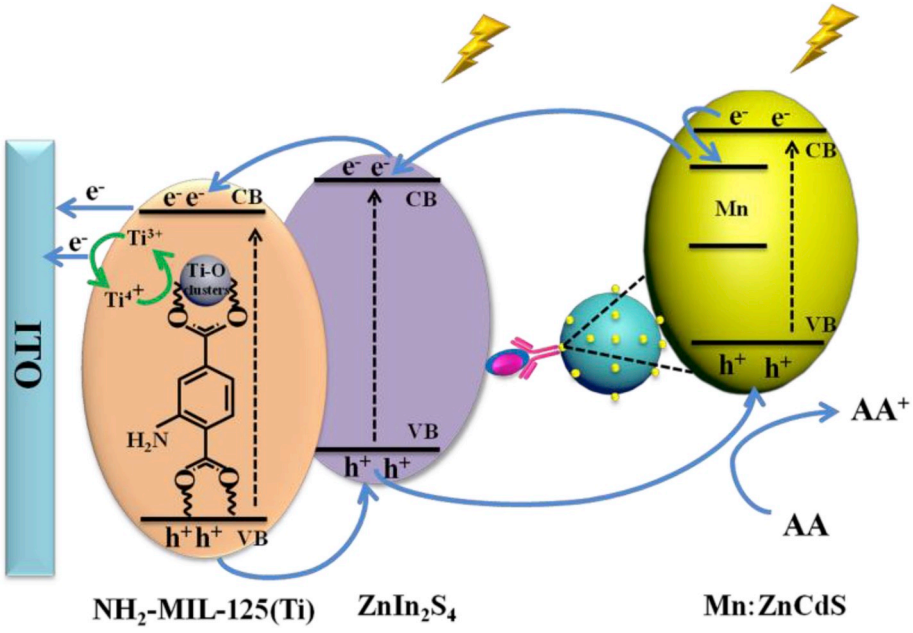


**Scheme 2.** The electron-transfer mechanism of the PEC immunosensor.

photocurrent intensity over $ZnIn_2S_4$@$NH_2$-MIL-125(Ti) composite increased with increasing $NH_2$-MIL-125(Ti) content and achieved a maximum at the dosage of $NH_2$-MIL-125(Ti) was 3%. However, when the dosage of $NH_2$-MIL-125(Ti) further increased, the photocurrent declined. It is inferred that excessive $NH_2$-MIL-125(Ti) may turn into a recombination center of photoinduced charges. The excitation wavelength and applied potential were discussed in Fig. S6, the optimal excitation wavelength was 450 nm (Fig. S6A). As the applied potential increased from −0.2 V to 0 V, the photocurrent reached 2.1 μA and later decreased when the applied potential further increased to +0.2 V (Fig. S6B). Thus, 0 V was used in this work. For Mn:ZnCdS QDs, the photocurrent intensity was affected by Cd:Zn ratio and the doping amount of $Mn^{2+}$. As displayed in Fig. S6C, the photocurrent reached a maximum when Cd:Zn ratio was equal to 9:1. Meanwhile, the photocurrent could be further improved by doping of $Mn^{2+}$, there was a maximal photocurrent intensity when the doping amount of $Mn^{2+}$ was 1% (Fig. S6D). As shown in Fig. 3B, the optimal concentration of PDA NS/Mn:ZnCdS QDs was 3 mg/mL.

Fig. 3C showed the effect of AA on the sensing performance. As an electron donor to trap the photogenerated holes, AA could suppress the $e^-/h^+$ recombination. The photocurrent was increased with AA concentration from 0.05 mol/L to 0.2 mol/L and reached a peak. Thus, 0.2 mol/L AA was used in this work. The influence of pH value on the photocurrent was also performed. As shown in Fig. 3D, the photocurrent increased from 6.5 to 7.4 and then decreased. Thus, the pH = 7.4 was chosen in this work. This could be contributed to that the immobilized protein can maintain their activity in neutral environment (Li et al., 2016; Liu et al., 2016). The effects of incubation time between mixing solution (free $E_2$ and PDA NS/Mn:ZnCdS-anti-$E_2$) and BSA-$E_2$ on the photocurrent response was shown in Fig. 3E. With the increasing of incubation time from 0.25 h to 1 h, the photocurrent increased and reached a stable level, indicating the mixing solution of free $E_2$ and PDA NS/Mn:ZnCdS-anti-$E_2$ has completely combined with BSA-$E_2$. Given this, 1 h was selected as the optimal incubation time.

### 3.5. PEC detection of $E_2$

Under the optimal conditions, the proposed PEC immunosensor was used to detect $E_2$. As shown in Fig. 4A, the concentration of $E_2$ was from 0.0005 ng/mL to 20 ng/mL. The photocurrent decreased gradually with the increment of $E_2$ concentrations. Fig. 4B displayed a good linear relationship between the reduction of photocurrent and the logarithm of $E_2$ at different concentrations. The equation of the calibration curve was $I = 1.483–1.01\ \lg c$, and the correlation coefficient was 0.994. The proposed PEC immunosensor displayed a wide response range and a low detection limit (0.3 pg/mL). As listed in Table S2, among most of previously reported methods for $E_2$ detection, the competitive-type PEC immunosensor possessed relatively good analytical performance and certain advantages in detection time (Zhang et al., 2019), which could realize the fast detection of target analytes in the future.

### 3.6. Stability, selectivity and reproducibility

To evaluate the stability of the competitive-type PEC immunosensor, the photocurrent responses were recorded with 10 on/off irradiation cycles. As shown in Fig. 4C, there was no obvious variation occurred, which suggested good stability of the proposed PEC sensors.

Selectivity was an important evaluation index for the application of an immunosensor. Some common interfering agents involving diethylstilbestrol, estriol and BSA were selected for the interference tests. It can be seen from Fig. 4D, upon the addition of 10 ng/mL other interfering substance in comparison with the biosensor incubated with 0.1 ng/mL $E_2$ only, no distinct interferential photocurrent signal was observed. The relative standard deviation (RSD) of photocurrent responses was 2.14% indicating a good selectivity of the competitive-type PEC immunosensor.

Reproducibility of the PEC immunosensor was assessed by measuring five electrodes (with 0.1 ng/mL $E_2$) under the same experimental condition. The PEC responses of measured five electrodes were 2.7, 2.68, 2.72, 2.8, and 2.65 with RSD of 2.09%. The above results indicated the acceptable reproducibility of this competitive-type PEC immunosensor.

### 3.7. Real sample analysis

To assess the analytical accuracy and the feasibility of immunosensor in practical application, the proposed PEC immunosensor was used to

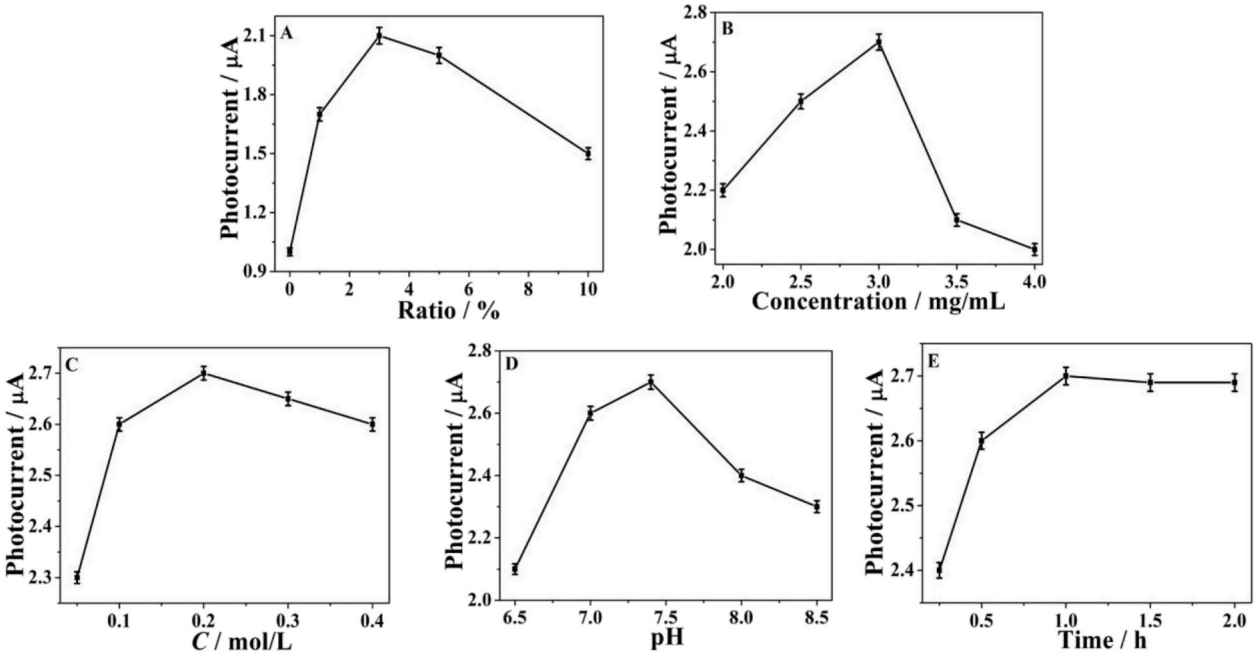


**Fig. 3.** The optimization of experimental conditions: (A) the dosage of $NH_2$-MIL-125(Ti); (B) concentration of PDA NS/Mn:ZnCdS QDs; (C) concentration of AA; (D) pH value; (E) the incubating time between the mixing solution (free $E_2$ and PDA NS/Mn:ZnCdS-anti-$E_2$) and BSA-$E_2$. $c_{E2} = 0.1$ ng/mL, Error bars = SD (n = 5).

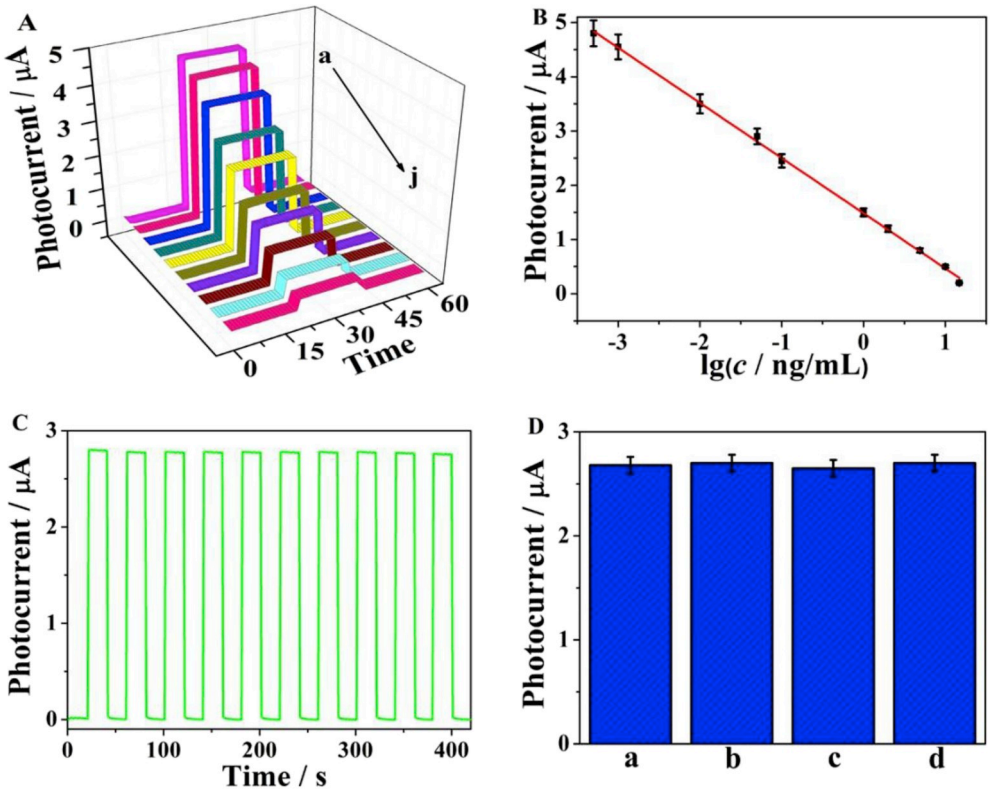


**Fig. 4.** (A) Photocurrent responses and (B) the logarithmic calibration curve of the competitive PEC immunosensor for the detection of different $E_2$ concentrations (from 0.0005 ng/mL to 20 ng/mL). (C) Stability of the sensor for the detection of 0.1 ng/mL $E_2$ under for 10 cycles. (D) The column of interference (a) 0.1 ng/mL $E_2$, (b) 0.1 ng/mL $E_2$ + 10 ng/mL diethylstilbestrol, (c) 0.1 ng/mL $E_2$ + 10 ng/mL estriol, (d) 0.1 ng/mL $E_2$ + 10 ng/mL BSA. Error bars = SD (n = 5).

detect the concentrations of $E_2$ in real water by standard addition methods. Initially, the $E_2$ in water samples was not detected. As shown in Table S3, three different concentrations of $E_2$ was added into lake water. The RSD was in the range of 2.7%–3.0% and recovery were 100.2%–100.8%. To further evaluate the selectivity of immunosensor in real sample analysis, 0.1 ng/mL $E_2$ containing 100-fold interfering substances were added to lake water. As shown in Fig. S7, no obvious photocurrent variation was observed when 10 ng/mL of diethylstilbestrol, estriol and BSA were incubated on the blank electrode respectively in the presence or absence of $E_2$. The analytical results indicated that the PEC immunosensor could be applied for the quantitative analysis of $E_2$ in real water.

## 4. Conclusions

In this study, $ZnIn_2S_4$@$NH_2$-MIL-125(Ti) nanocomposites with perfect PEC behavior were synthesized through a one-step solvothermal method and employed as photoactive matrix for the detection of $E_2$. Meanwhile, PDA NS/Mn:ZnCdS QDs was adopted as labels to amplify the PEC signal. The charge transfer of PDA NS and the favorable matching energy level between Mn:ZnCdS QDs and substrate dramatically improved the photocurrent response. Through the application of a competitive strategy, the obtained PEC immunosensor displayed a wide linear range (0.0005 ng/mL - 20 ng/mL) and a low detection limit of 0.3 pg/mL. The proposed PEC immunosensing platform with good stability, selectivity and reproducibility could provide a promising application for the detection of small molecules in environmental samples.

## Declaration of competing interest

The authors declare that they have no known competing financial interests or personal relationships that could have appeared to influence the work reported in this paper.

## CRediT authorship contribution statement

**Tao Yan:** Conceptualization, Data curation, Writing - original draft. **Tingting Wu:** Methodology, Writing - review & editing. **Shiyuan Wei:** Methodology, Writing - review & editing. **Haoqi Wang:** Methodology, Writing - review & editing. **Meng Sun:** Formal analysis, Methodology. **Liangguo Yan:** Investigation. **Qin Wei:** Funding acquisition, Project administration. **Huangxian Ju:** Funding acquisition, Project administration.

## Acknowledgments

This study was supported by the National Natural Science Foundation of China (21505051, 21575050, 21777056), National Key Scientific Instrument and Equipment Development Project of China (No.21627809), the Key Research and Development Program of Shandong Province (2016GSF117002), the Shandong Provincial Natural Science Foundation (ZR2016BQ12), the Special project of independent innovation and achievements transformation of Shandong Province (2014ZZCX05101), and QW thanks the Special Foundation for Taishan Scholar Professorship of Shandong Province (No. ts20130937) and UJN.

## Appendix A. Supplementary data

Supplementary data to this article can be found online at https://doi.org/10.1016/j.bios.2019.111739.

## References

Chen, Y.J., Huang, R.K., Chen, D.Q., Wang, Y.S., Liu, W.J., Li, X.N., Li, Z.H., 2012. ACS Appl. Mater. Interfaces 4 (4), 2273–2279.
Chen, S., Zeng, Q.Y., Bai, J., Li, J.H., Li, L.S., Xia, L.G., Zhou, B.X., 2017. Appl. Catal. B Environ. 218, 690–699.

Fan, G.C., Zhu, H., Shen, Q., Han, L., Zhao, M., Zhang, J.R., Zhu, J.J., 2015. Chem. Commun. 51 (32), 7023–7026.
Fan, D.W., Wang, H.Y., Khan, M.S., Bao, C.Z., Wang, H., Wu, D., Wei, Q., Du, B., 2017. Biosens. Bioelectron. 97, 253–259.
Feng, J.H., Li, F.Y., Li, X.J., Wang, Y.G., Fan, D.W., Du, B., Li, Y.Y., Wei, Q., 2018. Biosens. Bioelectron. 117, 773–780.
Fu, Y.H., Sun, D.G., Chen, Y.J., Huang, R.K., Ding, Z.X., Fu, X.Z., Li, Z.H., 2012. Angew. Chem. Int. Ed. 51 (14), 3364–3367.
Fu, Y.H., Sun, L., Yang, H., Xu, L., Zhang, F.M., Zhu, W.D., 2016. Appl. Catal. B Environ. 187, 212–217.
Han, Q., Xin, S., Zhu, W.Y., Zhu, C.H., Zhou, X.M., Jiang, H.J., 2016. Biosens. Bioelectron. 79, 180–186.
Han, Q.Z., Wang, R.Y., Xing, B., Zhang, T., Khan, M.S., Wu, D., Wei, Q., 2017. Biosens. Bioelectron. 99, 493–499.
Hao, Y., Gao, R., Shi, L., Liu, D., Tang, Y., Guo, Z., 2015. J. Chromatogr., A 1396 (3), 7–16.
He, H.W., Li, C.H., Tian, Y.F., Wu, P., Hou, X.D., 2016. Anal. Chem. 88 (11), 5892–5897.
Hendon, C.H., Tiana, D., Fontecave, M., Sanchez, C., D'arras, L., Sassoye, C., Rozes, L., Mellot-Draznieks, C., Walsh, A., 2013. J. Am. Chem. Soc. 135 (30), 10942–10945.
Jin, M., Mou, Z.L., Zhang, R.L., Liang, S.S., Zhang, Z.Q., 2017. Biosens. Bioelectron. 91 (7), 162–168.
Kampouri, S., Nguyen, T.N., Ireland, C.P., Valizadeh, B., Ebrahim, F.M., Capano, G., Ongari, D., Mace, A., Guijarro, N., Sivula, K., Sienkiewicz, A., Forró, L., Smit, B., Stylianou, K.C., 2018. J. Mater. Chem. A 6 (6), 2476–2481.
Li, Y., Dong, C.K., Chu, J., Qi, J.Y., Li, X., 2011. Nanoscale 3 (1), 280–287.
Li, X.J., Yu, S.Q., Yan, T., Zhang, Y., Du, B., Wu, D., Wei, Q., 2016. Biosens. Bioelectron. 89, 1020–1025.
Li, X.J., Wang, Y.G., Shi, L., Ma, H.M., Zhang, Y., Du, B., Wu, D., Wei, Q., 2017. Biosens. Bioelectron. 96, 113–120.
Li, X.Y., Pi, Y.H., Hou, Q.Q., Yu, H., Li, Z., Li, Y.W., Xiao, J., 2018. Chem. Commun. 54 (15), 1917–1920.
Lin, Y., Li, Z.H., 2014. Appl. Catal. B Environ. 160–161 (1), 552–557.
Liu, Y.X., Ma, H.M., Zhang, Y., Pang, X.H., Fan, D.W., Wu, D., Wei, Q., 2016. Biosens. Bioelectron. 86, 439–455.
Liu, H., Zhang, J., Ao, D., 2018. Appl. Catal. B Environ. 221, 433–442.
Ma, S., Simmons, J.M., Yuan, D., Li, J.R., Weng, W., Liu, D.J., Zhou, H.C., 2009. Chem. Commun. 27 (27), 4049–4051.
Ming, W.N., Wang, X.Y., Lu, W.H., Zhang, Z., Song, X.L., Li, J.H., Chen, L.X., 2017. Sens. Actuators B Chem. 238, 1309–1315.
Ouyang, J., Ripmeester, J.A., Wu, X., Kingston, D., Yu, K., Joly, A.G., Chen, W., 2007. J. Phys. Chem. C 111 (44), 16261–16266.
Peng, Y., Li, Y.S., Ban, Y.J., Jin, H., Jiao, W.M., Liu, X.L., Yang, W.S., 2014. Science 346 (6215), 1356–1359.
Shang, L., Zhou, C., Bian, T., Yu, H., Wu, L.Z., Tung, C.H., Zhang, T., 2013. J. Mater. Chem. A 1 (14), 4552–4558.
Shu, J., Qiu, Z., Zhou, Q., Lin, Y., Lu, M., Tang, D., 2016. Anal. Chem. 88 (5), 2958–2966.
Singh, A.C., Bacher, G., Bhand, S., 2017. Electrochim. Acta 232, 30–37.
Su, Y., Zhang, Z., Liu, H., Wang, Y., 2017. Appl. Catal. B Environ. 200, 448–457.
Sultana, S., Mansingh, S., Scurrell, M., Parida, K.M., 2017. Inorg. Chem. 56 (20), 12297–12307.
Tan, C.W., Zhu, G.Q., Hojamberdiev, M., Lokesh, K.S., Luo, X.C., Lei, J., Zhou, J.P., Peng, L., 2014. J. Hazard Mater. 278, 572–583.
Wang, H., Yuan, X.Z., Wu, Y., Zeng, G.M., Chen, X.H., Leng, L.J., Li, H., 2015. Appl. Catal. B Environ. 174–175 (3), 445–454.
Wang, H., Yuan, X.Z., Wu, Y., Zeng, G.M., Chen, X.H., Leng, L.J., Wu, Z.B., Jiang, L.B., Li, H., 2015. J. Hazard Mater. 286, 187–194.
Wang, R.Y., Ma, H.M., Zhang, Y., Wang, Q., Yang, Z.P., Du, B., Wu, D., Wei, Q., 2017. Biosens. Bioelectron. 96, 345–350.
Wang, X.P., Xu, R., Sun, X., Wang, Y.G., Ren, X., Du, B., Wu, D., Wei, Q., 2017. Biosens. Bioelectron. 96, 239–245.
Wu, D., Liu, Y.X., Wang, Y.G., Hu, L.H., Ma, H.M., Wang, G.Q., Wei, Q., 2016. Sci. Rep. 6, 20511.
Wu, T.T., Yan, T., Zhang, X., Feng, Y.X., Wei, D., Sun, M., Du, B., Wei, Q., 2018. Biosens. Bioelectron. 575–582.
Wu, T.T., Zhang, Y.R., Wei, D., Wang, X.D., Yan, T., Du, B., Wei, Q., 2018. Sens. Actuators B Chem. 812–819.
Xie, M., Yang, L., Ji, Y., Wang, Z., Ren, X., Liu, Z., Asiri, A.M., Xiong, X., Sun, X., 2017. Nanoscale 9 (43), 16612–16615.
Yan, J., Yang, L.P., Lin, M.F., Ma, J., Lu, X., Lee, P.S., 2013. Small 9 (4), 596–603.
Yuan, Y.J., Tu, J.R., Ye, Z.J., Chen, D.Q., Hu, B., Huang, Y.W., Chen, T.T., Cao, D.P., Yu, Z.T., Zou, Z.G., 2016. Appl. Catal. B Environ. 188, 13–22.
Zeng, X.X., Ma, S.S., Bao, J.C., Tu, W.W., Dai, Z.H., Chem, A., 2013. Anal. Chem. 85 (24), 11720–11724.
Zhan, W.W., Kuang, Q., Zhou, J.Z., Kong, X.J., Xie, Z.X., Zheng, L.S., 2013. J. Am. Chem. Soc. 135 (5), 1926–1933.
Zhang, X.Y., Peng, Y., Bai, J.L., Ning, B.A., Sun, S.M., Hong, X.D., Liu, Y.Y., Liu, Y., Gao, Z.X., 2014. Sens. Actuators B Chem. 200 (3), 69–75.
Zhang, G.Y., Zhuang, Y.H., Dan, S., Su, G.F., Cosnier, S., Zhang, X., 2016. Anal. Chem. 88 (22), 11207–11212.
Zhang, K.Y., Lv, S.Z., Lin, Z.Z., Tang, D.P., 2017. Biosens. Bioelectron. 95, 34–40.
Zhang, Y., Liu, Y., Ma, M., Ren, X., Liu, Z., Du, G., Asiri, A.M., Sun, X., 2017. Chem. Commun. 53 (80), 11048–11051.
Zhang, Y.F., Wang, M.D., Wang, Y.G., Feng, J.H., Zhang, Y., Sun, X., Du, B., Wei, Q., 2019. Biosens. Bioelectron. 126, 23–29.
Zhao, W.W., Chen, R., Dai, P.P., Li, X.L., Xu, J.J., Chen, H.Y., Chem, A., 2014. Anal. Chem. 86 (23), 11513–11516.